Deformation of olivine in torsion under hydrous conditions

Sylvie Demouchy, Andrea Tommasi, Fabrice Barou, David Mainprice, Patrick Cordier

Deformation of olivine in torsion under hydrous conditions

Sylvie Demouchy [a,*], Andréa Tommasi [a], Fabrice Barou [a], David Mainprice [a], Patrick Cordier [b]

[a] Geosciences Montpellier, Université Montpellier 2 & CNRS, UMR 5243, Montpellier, France
[b] Unité Matériaux et Transformations, Université Lille 1 & CNRS, UMR 8207, Villeneuve d'Ascq, France

We performed torsional deformation experiments on pre-hydrated fine-grained olivine aggregates using an innovative experimental assembly to investigate water weakening in mantle rocks at high shear strains. San Carlos olivine powder was cold-pressed and then hot-pressed under hydrous conditions, producing aggregates with average grain sizes of 7 or 15 μm. Deformation experiments were performed in a high-resolution gas-medium apparatus equipped with a torsional actuator, under a confining pressure of 300 MPa, a temperature of 1200 °C, and constant shear strain rates ranging from 8×10^{-5} to 1.4×10^{-4} s^{-1}. Maximum shear stresses range from 150 to 195 MPa. These values are 30% lower relative to those determined in previous torsion experiments on dry, fined-grained dunites under similar conditions. Textures and microstructures of the starting and deformed specimens were characterized by scanning and transmission electron microscopy. All deformed aggregates exhibit a shape-preferred orientation marking a foliation and lineation, as well as a reduction in mean grain size from 15 μm down to 3–4 μm due to dynamic recrystallization. Olivine crystallographic fabrics developed rapidly ($\gamma < 0.1$), but their strength, characterized by the J-index, is low compared to naturally deformed peridotites or to polycrystalline olivine deformed at similar finite shear strains under dry conditions. The crystallographic fabrics are consistent with deformation by a dislocation accommodated creep mechanism with activation of multiple {0*kl*}[100] systems, among which the (010)[100] slip system is dominant, and minor participation of the (010)[001] slip system. Transmission electron microscopy confirmed the occurrence of dislocations with [100] and [001] Burgers vectors in most grains. Analysis of unpolarized infrared spectra indicates that hydrogen concentration in the olivine lattice is below the saturation level of 18 ppm wt H_2O, which is similar to those typically observed in spinel-bearing peridotite xenoliths, and also provide evidence for water-rich inter-granular material trapped in pores and grain boundaries. Seismic properties computed from the CPO observations correspond to those most commonly observed in naturally deformed mantle peridotites with fast P-wave propagation and S-wave polarization subparallel to the shear direction. These torsion experiments on fine-grained olivine polycrystals under hydrous conditions indicate that water weakening under lithospheric conditions is linked to various defects with hydrogen in the olivine structure, as well as with water-derived species in grain boundaries or pores.

1. Introduction

Major faults may extend into the mantle as ductile shear zones, where localized deformation takes place essentially by simple shear. Mantle shear zones are observed in peridotite massifs and in seismic profiles, and their presence is also inferred based on seismic and electrical anisotropy data (cf. recent review by Vauchez et al., 2012). Yet estimations of shear zones width and distribution at different depths in the upper mantle based on these observations are highly contrasted.

The strength of the mantle lithosphere and the degree of strain localization are essentially controlled by the rheological properties of the mineral olivine, which represents 60–80% of the upper mantle volume and is the only mineral phase being interconnected and thus acting as a stress-bearing frame. At high temperatures (>1200 °C), the rheological behavior of natural and synthetic olivine-rich rocks (dunites) is well described by a power-law equation, which expresses the strain rate ($\dot{\varepsilon}$) as a function of thermomechanical and microstructural parameters as follows:

$$\dot{\varepsilon} = A\sigma^n d^{-p} f_{H_2O}^r \exp(\alpha\phi) \exp\left(-\frac{Q + P\Delta V^*}{RT}\right) \quad (1)$$

where A is a material-dependant constant, σ is the differential stress, n and p are the stress and grain size exponents, d is the grain size, f_{H_2O} is the water fugacity, r is the water fugacity exponent, ϕ is

* Corresponding author. Address: Géosciences Montpellier, Université Montpellier 2 & CNRS, cc060, Place Eugène Bataillon, 34095 Montpellier cedex 5, France. Tel.: +33 (0)467 14 49 42 (office), +33 (0)467 14 36 07 (lab); fax: +33 (0)467 14 36 03.

E-mail address: demouchy@gm.univ-montp2.fr (S. Demouchy).

the melt fraction, α is a constant, Q is the activation energy, ΔV is the activation volume, R is the gas constant, P is the pressure, and T is the absolute temperature. In this semi-empirical equation, the A, n, p, r, Q, ΔV, and α parameters are experimentally determined. Over the past decade, experimental studies have extensively worked on their determination (e.g., Hirth and Kohlstedt, 2003; Kohlstedt, 2007; Karato, 2008; Mackwell, 2008; Zhao et al., 2004; Demouchy et al., 2009; Keefner et al., 2011; Hansen et al., 2011). Moreover, under hydrous conditions, the combination of diffusion creep and dislocation creep mechanisms in olivine at constant pressure and temperature can be expressed by the so-called constitutive equation (Hirth and Kohlstedt, 2003),

$$\dot{\varepsilon}_{\text{wet const. eq}} = \dot{\varepsilon}_{\text{wet diff}} + \dot{\varepsilon}_{\text{wet dis}} = A_{\text{wet dis}}\sigma^{3.5} + A_{\text{wet diff}}\sigma d^{-3} \quad (2)$$

In parallel, the deformation mechanisms and slip systems in olivine at high temperature and confining pressure were well documented by electron microscopy (e.g., Phakey et al., 1972; Bai and Kohlstedt, 1992; Couvy et al., 2004). Though, almost all previous experiments were performed in compression to strains of less than 20%, which corresponds to a shear strain $\gamma < 0.35$ (with $\gamma = (\frac{\theta D}{2l})$, where D the sample diameter, l the sample length and θ the angular displacement) (e.g., Bai and Kohlstedt, 1992; Couvy et al., 2004). At high shear strains ($\gamma \gg 1$) appropriate for shear zones in the Earth's lithosphere, significantly fewer data on olivine rheology are available (Bystricky et al., 2000; Kawazoe et al., 2008). Large strain deformation experiments are only now reaching maturity due to significant technical improvements particularly those associated with torsion tests at high pressures and temperatures (Paterson and Olgaard, 2000). Deformation in a torsional geometry has many advantages relative to traditional tri-axial mechanical tests as it permits larger finite strains ($\varepsilon \gg 0.2$) and avoids boundary effects at both ends of the sample and thus barreling of the sample.

This new deformation apparatus for torsion allowed investigation of the evolution of the microstructures and textures up to large shear strains as well as the effect of this evolution on the rheological behavior of calcite aggregates (Casey et al., 1998; Paterson and Olgaard, 2000; Pieri et al., 2001; Barnhoorn et al., 2004, 2005; Delle Piane et al., 2008), serpentinites (Hirose et al., 2006), bi-mineralic aggregates (Larkin et al., 2005; Bystricky et al., 2006), ferropericlase (Heidelbach et al., 2003, 2009), and melt-solid aggregates (Kohlstedt et al., 2010; King et al., 2009, 2011a, 2011b). For dry fine-grained olivine aggregates, few experiments involving high shear stresses by torsion were performed successfully at the limits (mainly stress, temperature, and pressure) of the possible experimental conditions (Bystricky et al., 2000).

The present study examines the effect of water on the shear deformation of polycrystalline olivine in a torsional gas-medium deformation apparatus with an innovative sample assembly, in which an internal porous alumina reservoir provides hydrogen to the sample during the experiment. The results of our experiments are compared to previous high-temperature torsion results on dry polycrystalline aggregates of olivine (Bystricky et al. 2000) as well as to data from tri-axial compressive creep tests performed under both dry and wet conditions (Mei and Kohlstedt, 2000). This study provides new constraints on the nature and effect of water on the deformation behavior of Earth's lithospheric mantle.

2. Experimental methods

2.1. Sample preparation

Olivine grains with minimal alteration (less than 3% of the surface), selected from peridotite xenoliths from San Carlos (Arizona, USA, with chemical composition close to $Mg_{0.904}Fe_{0.092}Ni_{0.0035}Cr_{0.0003}SiO_4$, $\sim Fo_{90}$), were tumbled and washed to remove surface weathering products before being reduced to a fine powder using a fluid energy mill as described in Mei and Kohlstedt (2000). The resulting particle size ranged from 1 to 20 μm. The olivine powder was first cold pressed at 100 MPa into a thick wall Ni canister (26 mm long, 11.7 mm outside diameter, 10 mm inside diameter). The Ni canister was closed with a fitted Ni lid and was encapsulated along with zirconia pistons, alumina pistons and alumina spacers in an iron jacket as detailed in Demouchy et al. (2009). The cold-pressed sample was afterwards annealed under a confining pressure of 300 MPa and at a temperature of 1250 °C for 3 h (hot-press step). Two types of hot-pressed samples were prepared (Table 1): (1) those with 30 μL of filtered and deionize water (Milli-q grade) added to the cold-pressed aggregate and with no axial force was applied during the hot pressing step (run PI-1619) and (2) those with 45 μL of deionized water added to the cold-pressed aggregate and a small axial force of 0.3 kN (≈4 MPa) was applied during the last hour of the hot press (run PI-1620).

An innovative setup was designed to provide additional water during at least part of the torsion experiment (Fig. 1). First, the former iron jacket and nickel sleeve of the hot-pressed sample were reduced on a lathe to an external diameter of ~9.9 mm to fit into a new iron jacket. The central part of the cylindrical dense polycrystalline olivine was then removed with a diamond core-drill. Second, a double internal Ni capsule (with a length of 5 mm, an outer diameter of 5 mm, and a inner diameter of 4 mm, similar in principle to the 'telescopic' capsule described in Chen et al., 2006) containing a plug of porous alumina (with 19% interconnected porosity) which itself contained 20 μL of deionized water (i.e., water was added using a microsyringe, step by step, with increment of 5 μL) and was placed in the central hole of the olivine aggregate. The double internal nickel container ensures that no aqueous fluid infiltrates from the porous alumina toward the rest of the assembly and thus only allows continuous hydrogen diffusion from the porous alumina reservoir to the olivine aggregate through the Ni during the torsion experiment. Estimates of hydrogen diffusion through nickel suggest that only ~3 s are necessary for hydrogen to diffuse through the Ni wall ($D_H^{in\ Ni} = 8 \times 10^{-8}\ m^2\ s^{-1}$ at 1200 °C; Wimmer et al., 2008). Ni was chosen to fix the oxygen fugacity near the Ni–NiO buffer during both annealing and torsion experiments yielding a $f_{O_2} \approx 10^{-2.6}$ Pa at 300 MPa and 1200 °C (O'Neill and Wall, 1987). A porous alumina reservoir loaded with water was preferred to talc or brucite as it avoids the drastic volume change associated with water release due to breakdown of these hydrous minerals at temperature above 800 °C temperature. The torsion sample assembly was then encapsulated in an iron jacket along with alumina spacers as well as zirconia and alumina pistons. Porous coarse-grained alumina spacers were placed above and below the olivine aggregate as described by King et al. (2009). A detailed sketch of the multipart canister is provided in Fig. 1a.

2.2. Torsion experiments

Four torsion deformation experiments were performed using a high-resolution gas-medium high-pressure torsion apparatus (Paterson and Olgaard, 2000). First, the samples were annealed for 1 h to permit hydrogen to diffuse into the sample and to allow creep of the olivine aggregate into the asperities on the surface of the coarse-grained porous alumina spacers in order to obtain a better coupling between the olivine aggregate and the porous alumina spacers located immediately above and below the sample (Fig. 1a and b). For runs PI-0546 and PI-0546, a force of 1 kN (≈16 MPa) was applied during the annealing stage, before starting the torsion, whereas samples PI-0544 and PI-0545 were annealed under hydrostatic conditions before torsion.

Table 1
Experimental conditions, resulting grain size, water contents for hot-press and torsion experiments, and mechanical data.

Run #	Starting material	Pressure (MPa)	Duration (min)	Sample length (mm)	Sample diameter (mm)	Grain size range and (average) [c] (μm)	Water content[d] ppm wt. H_20	Shear strain rate[e] $\dot{\gamma}$ (Eq. strain rate $\dot{\varepsilon}$ s^{-1})	Calculated total shear strain γ	Max shear stress τ (Max eq. stress ε) (MPa)
Hot press experiments at 1250 °C										
PI-1619	Powder	300	180	26	10	2–18 (6.6)	Broad band	–	–	–
PI-1620[a]	Powder	300	180	26	10	3–44 (14.7)	13 ± 7 + Broad band	–	–	–
Dextral shear experiments at 1200 °C										
PI-0544	PI-1619	300	31	5.08	8.41	0.6–25 (4.2)	n.d.	1.4×10^{-4} (7.9×10^{-5})	0.26[g]	212 (338)
PI-0545	PI-1619	300–274[b]	17	4.62	8.41	0.6–33 (5.2)	n.d.	2.9×10^{-4} (1.6×10^{-4})	0.29[g]	195 (367)
PI-0546[a]	PI-1620	300–288[b]	527	5.28	8.92	0.6–65 (4.5)	Broad band	7.3×10^{-5} (4.6×10^{-5})	2.31	151 (264)
PI-0548[a]	PI-1620	300	633	5.04	8.92	0.56–45 (3.8)	Broad band	[f]8.0×10^{-5} (4.6×10^{-5})	3.04	159 (248)

[a] Small load was applied during annealing (0.3–1 kN).
[b] Confining pressure slowly decreased during torsion experiments, but pressure lost was limited (less than 30 MPa).
[c] True grain size range and average grain size. True average diameter of grains $d = K_1 \times L$, where K_1 is a constant depending on the grain shape equals to 1.5 for equidimentional grains and L is the mean interval between two grain boundaries (i.e., equivalent to the mean apparent grain size obtained using EBSD maps), see Etheridge and Wilkie (1981) and Vauchez (1987) for details.
[d] Water content was obtained using the calibration of Paterson (1982) from unpolarized infrared radiation; uncertainties are ±30%. n.d. = Not detected.
[e] Equivalent strain rate and equivalent stress can be calculated according to Paterson and Olgaard (2000) with $\dot{\varepsilon} = \dot{\gamma}/\sqrt{3}$ and $\sigma = \tau\sqrt{3}$, respectively.
[f] Shear strain rate was found to regularly increase from 5.3×10^{-5} to 9.9×10^{-5} s^{-1} over time despite a fix angular displacement rate.
[g] Shear strain rate for the steady state portion only, that is before slip at boundaries occurred.

All experiments were performed at a constant angular rotation rate at T = 1200 °C. The uncertainty on the measurement of the shear stress is less than 5 MPa. The maximum confining pressure was 300 MPa. During the experiments, temperature was monitored using a $Pt–Pt_{0.87}Rh_{0.13}$ thermocouple placed 6 mm above the top of the sample; previous calibration runs indicate that temperature varies by less than 2 °C along the length of the sample. The temperature was increased at a rate of ~30 °C/min at the beginning of the experiment. At the end of an experiment, temperature was decreased to 300 °C within 16 min.

To determine the contribution to the total torque of the force supported by the iron jacket, the external nickel sleeve, and the internal Ni double capsule, we used published flow laws for iron and nickel (Frost and Ashby, 1982). Since nickel is significantly weaker than olivine at 1200 °C, the central Ni capsule supports a negligible torque (i.e., our assembly effectively behaves as a hollow cylinder, see Paterson and Olgaard (2000) for details). Because the porous alumina plug is entirely encapsulated in weak nickel, its contribution to the torque is assumed to be negligible as well. Finally, an initial value for the stress exponent of n = 3.5 was taken (as in Eq. (2)) for the data analysis based on flow law for dislocation creep from Hirth and Kohlstedt (2003) and in agreement with King et al. (2009).

2.3. Fourier transform infrared analysis

OH^- content was determined using Fourier transform infrared (FTIR) spectroscopy to quantify the amount of hydrogen incorporated as point defects in the olivine crystallographic structure and to define its speciation. Analyses were performed with a Bruker FTIR spectrometer coupled with a Hyperion microscope as in Demouchy (2010b). Analyses were made at room temperature and pressure, under a stream of H_2O– and CO_2–free purified air flowing though the microscope. Middle infrared measurements were performed using a Globar light source, a KBr/Ge beam splitter and high-sensitivity, narrow-band MCT (mercury-cadmium-telluride) detector cooled by liquid nitrogen. Unpolarized radiation and a square aperture of 50 or 80 μm were used; 200–800 scans were accumulated at a resolution of 4 cm^{-1}. Measurements were acquired on the hot-pressed starting material and on each torsion sample both at ~100 μm from the Ni external sleeve and at ~100 μm from the internal Ni capsule. Cracks resulting from quenching or sample preparation were strictly avoided; nevertheless due to the small grain size (≪100 μm), grain boundaries could not be avoided and all spectra were slightly affected by diffraction from grain boundaries, which results in decrease of signal to noise ratio. After background correction, each FTIR spectrum was baseline rectified and normalized to 1 cm of thickness. The OH^- content was determined using the calibration of Paterson (1982):

$$C_{OH} = \frac{\phi_i}{150\xi} \int \frac{k(v)}{3780 - v} dv \quad (3)$$

where C_{OH} is the concentration of hydroxyl, ξ is the orientation factor equals 1/3 for unpolarized measurements, and $kv(v)$ is the absorption coefficient for a given wavenumber v. The density factor ϕ_i, is chemistry dependent and equals 2695 ppm wt. H_2O for olivine Fo_{90} (the method for calculation of ϕ_i is given in Bolfan-Casanova et al., 2000). Although this calibration may underestimate the water content for olivine (Bell et al., 2003), we choose it to facilitate comparison with previous studies (e.g., Mei and Kohlstedt 2000; Jung and Karato 2001a; Hirth and Kohlstedt, 2003). In addition, the olivine grain size in the experimental samples is too small to perform polarized infrared measurements on crystallographically oriented grains, which are required to apply the more recent calibration from Bell et al. (2003).

2.4. Texture characterization

We analyzed the microstructure of both the starting hot-pressed material and the sheared specimens using scanning electron microscopy (SEM). Statistical quantification of the crystallographic preferred orientations (CPO) was performed by analysis of electron-backscattered diffraction (EBSD) patterns. For the starting material, sections parallel to the basal section of the cylinders were prepared (perpendicular to the vertical cylinder axis). For the sheared samples, two sections were cut: (i) one parallel to and near the cylinder long axis (referred to as axial sections) and (ii) one tangential to the external boundary of the sample cylinder (tangential sections). Both sections are perpendicular to the shear plane, although the axial section is normal to the shear direction and the tangential section is nearly parallel to it. To ensure high-quality SEM imaging and EBSD analyses, after mechanical polish-

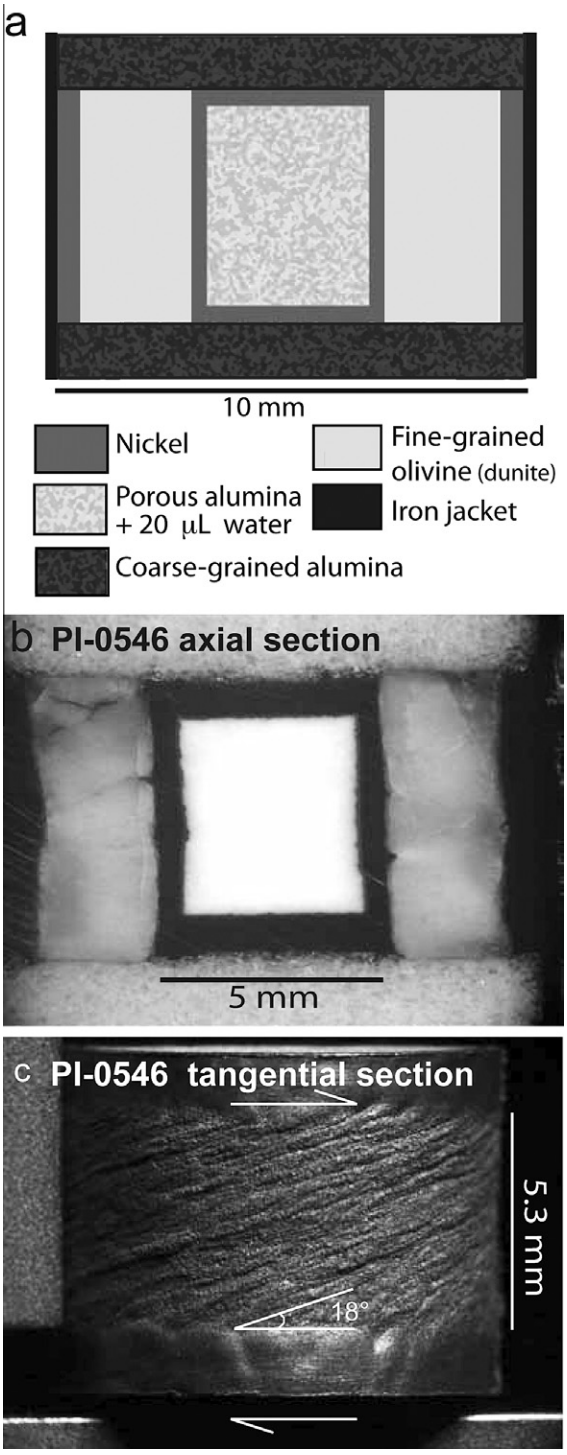

Fig. 1. (a) Sketch of the torsion assembly, (b) photography of axial section of sample PI-0546 after torsion and (c) photography of the external iron jacket of sample PI-0546 after torsion showing the dextral shearing of the assembly.

ing with diamond paste, a final polishing with colloidal silica suspension was performed to remove the damage in near surface layers introduced by mechanical polishing. EBSD analyses were conducted with a CamScan X500FE CrystalProbe equipped with an EBSD system at Geosciences Montpellier (France). The operating conditions were a current of 25 kV and 3.5 nA and a working distance of 20 mm. Low vacuum conditions (5 Pa of gaseous nitrogen) were used to avoid charging of the samples. The detailed geometry of the CrystalProbe-EBSD is given in Demouchy et al. (2011); its principal particularity is that the incoming electron beam is at an angle of 20° to the horizontal sample stage. Data were acquired and treated with CHANNEL5 software.

Crystal orientation maps acquired on the starting material have a sampling step size of 0.5 μm and cover 1/3 of the basal section. The areas mapped were 300 × 130 μm in size. Both axial and tangential sections of all sheared samples were investigated, although different map sizes and sampling steps were used for the four sheared samples. For runs PI-0544 and PI-0545, half of each axial section was analyzed (1800 × 5100 μm maps with a step size of 5 μm). For the two other runs, only a small horizontal band (perpendicular to the shear direction) of each axial section was analyzed, which yielded a smaller maps of 1860 × 160 μm with a step size of 0.6 μm for PI-0548 and 1600 × 70 μm with a step size of 0.3 μm for PI-0546. These axial sections maps were subsequently divided in intervals ∼100 μm wide parallel to the shear plane, with more than 150 grains per map measured in each interval, to study the evolution of the fabric with increasing shear strain; each interval corresponds to ∼1/20 of the total finite shear strain reached in the experiment (Table 1). For the tangential sections, several mapping strategies were tested. For run PI-0546, both a long thin horizontal map (700 × 75 μm with a step size of 0.3 μm and the long dimension parallel to the shear direction) and a long thin vertical map (50 × 1200 μm with a step size of 0.3 μm and long dimension normal to the shear plane) were performed. For PI-0548, a square map (200 × 165 μm with a step size of 0.3 μm) as well as large rectangular maps (500 × 400 μm with a step size of 0.6 μm) were acquired. Maps required 24–60 h of data acquisition. Despite the different step sizes and map shapes, the measured olivine CPOs in each tangential section of the sheared olivine aggregates are identical. Raw indexation rates were between 67% and 81%. Data treatment allowed the non-indexed pixels to be filled, if up to eight identical neighbors existed with this orientation; this operation was repeated using respectively seven and six identical neighbors (yielding to post-treatment indexation rates >92%). The processed data were used to identify grains by defining a pixelated area with an internal misorientation <10°. The data set was then reduced to one point of measurement per grain in order to limit potential oversampling of rare abnormally large grains. A minimum of 100 grains was always analyzed in each interval or section, ensuring a good statistical analysis of the CPOs and grain sizes and shapes.

CPOs are plotted as pole figures showing the orientation of the main crystal axes ([100], [010] and [001]) relative to the sample coordinates using the PFch5 software (Mainprice and Silver, 1993). The discrete point distributions of Euler angle triplets (i.e., orientation distribution function ODF) are converted into densities by grouping them within 1° ODF cells and then smoothing with a Gaussian function with 8.5° full-width-at-half-maximum. The resulting density distributions were then normalized and contoured. The texture J-index, which is the volume-averaged integral of squared orientation densities (Bunge, 1982), was then calculated using the SuperJctf software (see Mainprice and Silver, 1993; ftp://www.gm.univ-montp2.fr/mainprice//CareWare_Unicef_Programs/) using a 10° Gaussian half-width, data at 1° bins, and truncation of the orientation distribution function (ODF) at 22°.

2.5. Transmission electron microscopy observations

We used transmission electron microscopy (TEM) to characterize the deformation microstructures. Doubly polished thin sections were prepared from the tangential section of the recovered specimens for TEM observation. The samples were glued on a Mo grid and ion milled at 5 kV under a beam angle of 15° until electron transparency was reached. TEM observations were carried out using a Philips CM30 microscope operating at 300 kV. Crystal orientation and diffraction vector selection were achieved by using

selected-area electron-diffraction and precession electron diffraction with a "Spinning Star" precession module.

3. Results

3.1. Olivine starting material

Characterization by SEM of the olivine starting material (basal section) reveals that the two hot-pressed experiments have different starting microstructures (Fig. 2 and Table 1). PI-1619 has an average grain size of 6.6 μm and is macroscopically pale gray, while PI-1620 underwent extensive grain growth yielding an average grain size of 14.7 μm with a noteworthy celadon green color. The difference in macroscopic color is likely due to the difference in grain size (Karato et al., 1986; Karato, 1990) and associated with difference in the number of grain boundaries. The larger grain size in sample PI-1620 relative to PI-1619 is consistent with the higher starting intra-crystalline water content together with enhanced grain boundary migration induced by the 2 MPa of differential stress applied during the hot-press of PI-1620. Triple junctions with 120° angles are visible in both samples, which also show numerous curved boundaries as illustrated in Fig. 2. The average aspect ratio of the olivine grains is ~1.6 for both starting material aggregates.

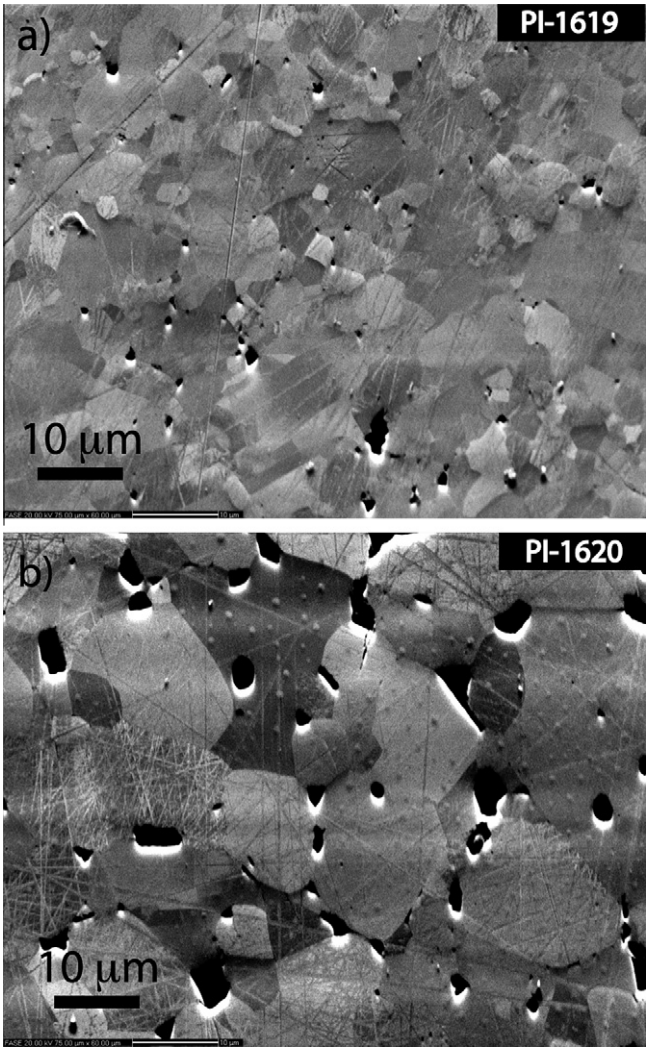

Fig. 2. Backscattered-electron images using SEM of the olivine starting material after hot pressing and prior to torsion indicating differences in grain size between (a) sample PI-1619, and (b) sample PI-1620. Dark areas are porosity and plucks out from polishing.

Pole figures and J-indexes for all crystallographic axis for sample PI-1620 sample are presented in Fig. 3 and reveal a weak axial symmetry in the CPO with [100] and [001] forming a faint girdle normal to the cylinder axis and [010] defining a weak maximum parallel to the cylinder axis. Sample PI-1619 also has a weak CPO, but with a less-developed axial symmetry and lower densities. In both samples, [010] axes form a weak maximum parallel to the cylinder axis, and are more concentrated than [100], which is more concentrated than [001].

Unpolarized FTIR spectra from olivine aggregates obtained from slabs with thicknesses between 370 and 550 μm confirmed the presence of small amounts of water in the starting materials as illustrated in Fig 4. The FTIR spectra for olivine in sample PI-1620 have a large broad band centered at 3450 cm^{-1} as well as sharply defined peaks at 3570, 3361, and 3331 cm^{-1}. These narrow peaks located above the broad band are characteristic of high-pressure hydrogenated olivine grains (later called water *sensus stricto* in olivine) and are similar to FTIR spectra reported in previous experimental studies on olivine single crystals (e.g., Mackwell et al., 1985; Demouchy and Mackwell, 2006).

The large broad band centered at 3450 cm^{-1} is commonly observed in fine-grained synthetic olivine aggregates hydrated at moderate pressures (0.2–1 GPa) as well as in natural dunites (e.g., Chopra and Paterson, 1984; Karato et al., 1986, Mei and Kohlstedt, 2000; Zimmerman and Kohlstedt, 2004; Faul and Jackson, 2007; Aizawa et al., 2008). A broad band at similar wavenumbers was usually attributed to free molecular water (e.g., Aines and Rossman, 1984; Bell et al., 2003; Mosenfelder et al., 2011), which we assume could be trapped in pores. Alternatively, grain boundaries and nano-scale water-rich intra-granular inclusions were also proposed as the origin of such broad band (Keppler and Rauch, 2000).

To estimate the water content in the olivine structure, we executed a decomposition of the spectrum using an algorithm combining multiple Lorentzian functions (Cauchy distribution) and Gaussian functions (provided by the IR spectrometer OPUS software for data acquisition and treatment), which allowed for removal of most of the broad band centered at 3450 cm^{-1}. The water contents of the olivine structure in the starting material can then be estimated based only on the narrow peaks at 3570, 3361, and 3331 cm^{-1}. They differ between the two runs and range from 3 to 13 ± 7 wt. ppm H_2O (Table 1). Note that the removal of the large broad band introduces large uncertainties in the resulting water content in olivine as any additional data treatment does. However, the estimated water contents are slightly below the saturation concentrations reported for undeformed iron-bearing olivine by Zhao et al. (2004) at similar confining pressure, temperature and water fugacity. They are also within the range of values observed in natural mantle-derived spinel-bearing peridotites for similar pressure and temperature conditions (e.g., Miller et al., 1987; Soustelle et al., 2010).

3.2. Mechanical data

Four samples were sheared at high pressure at 1200 °C at constant angular displacement or twist rate (Table 1). In the first two experiments (PI-0544 and PI-0545, samples with no annealing before torsion) slip occurred after a shear strain of ~0.25, on the interface between the sample and the lower porous alumina spacer. The maximum shear stress, which can be supported by such interfaces can be calculated based on its frictional strength and is described by the relationship $\tau_{max} = \frac{1}{3}\mu P(3 + n^{-1})$, where μ the friction coefficient is ~0.5, P is pressure, and n was experimentally determined and equals ~3.5 (Paterson and Olgaard, 2000). This analysis yields $\tau_{max} \approx 170$ MPa, a value exceeded in these experiments. After slipping initiated at a shear strain of ~0.25, the shear stress decreased rapidly with time, then it stabilized for more than 4 h before a drastic decrease leading to the

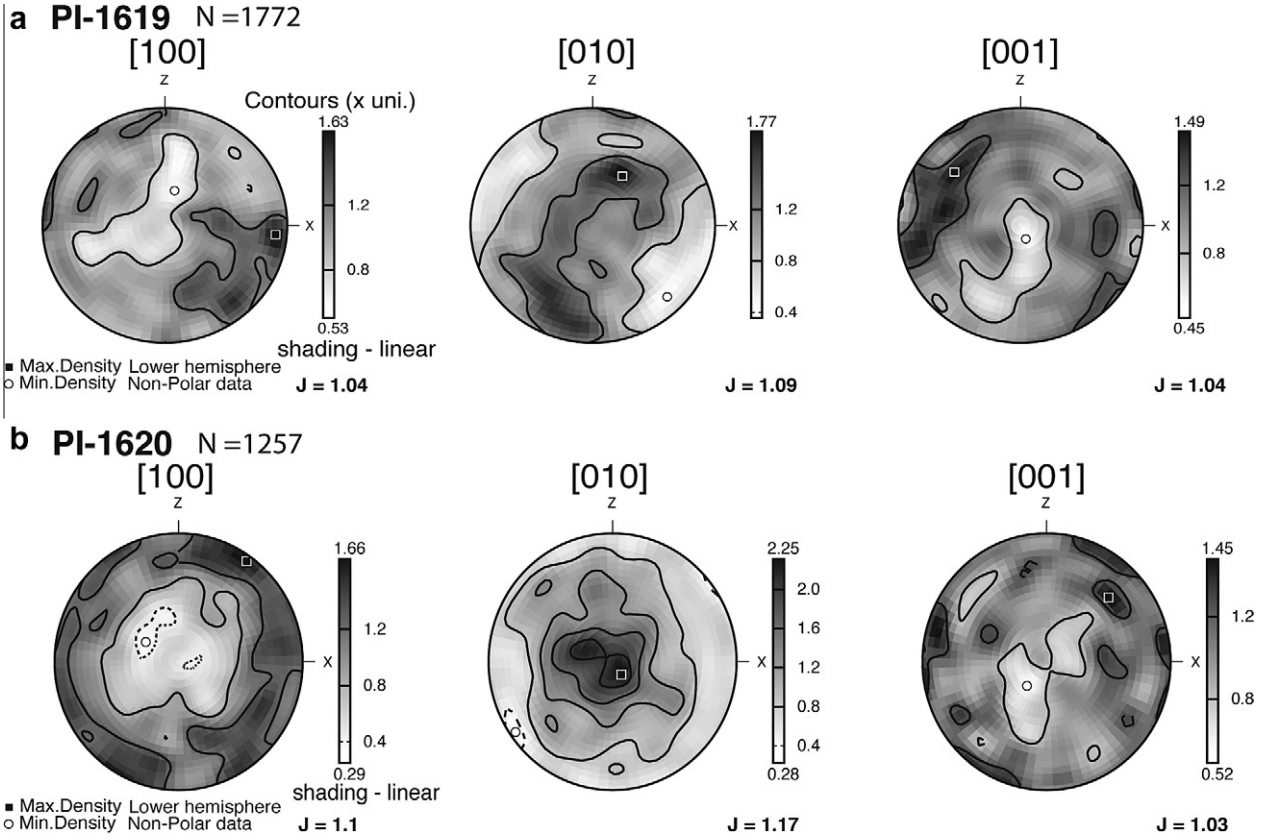

Fig. 3. Crystallographic preferred orientations (a) sample PI-1619 and (b) sample PI-1620 after annealing at high pressure and prior to torsion. Pole figures are in lower hemisphere equal-area projections. N is the number of analyzed olivine grains. Maximum and minimum density contours are given at the top and bottom of the color linear scale respectively. Low J-indexes ($J \approx 1$) indicating the quasi absence of rock fabric. The cylindrical axis of the sample is perpendicular to the page.

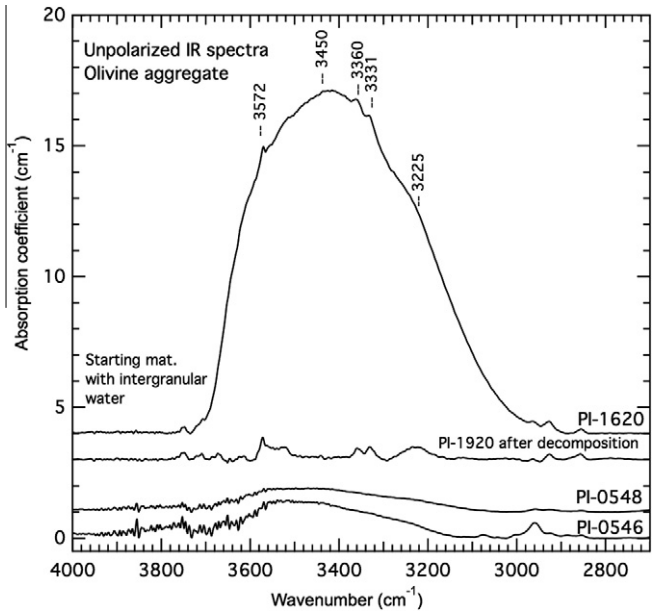

Fig. 4. Unpolarized FTIR spectra for the olivine aggregate starting materials and the deformed olivine samples, which show characteristic IR bands for low-pressure hydrogenated olivine and a large broad band attributed to inter-granular (in pores and grain boundaries) water-derived species. All spectra are normalized to a thickness of 1 cm.

termination of the experiments (see Fig. S1 in the online Supplementary material). Therefore, only the short steady state portions ($0< \gamma <0.25$) for these two experiments (PI-0544 and PI-0545) are shown in Fig. 5A.

The two subsequent torsion experiments (PI-0546 and PI-0548) were successfully twisted to a shear strain of $\gamma \approx 3$ at a slower constant angular displacement rates and thus reached lower maximum shear stresses (Table 1 and Fig. 5A). The mechanical results are represented as shear stresses (τ) as a function of shear strain (γ) and also as Von Mises equivalent stresses and strains in Fig. 5A. The latter facilitates comparison with results from tri-axial tests in compression ($\sigma_{eq} = \sqrt{3}\tau$ and $\dot{\varepsilon}_{eq} = \frac{1}{\sqrt{3}}\dot{\gamma}$ as in Paterson and Olgaard, 2000). The variation between the minimum shear stress (i.e., internal layer of olivine) and the maximum shear stress (i.e., external layer) as a function of shear strain is only of 20 MPa (with a ratio $\tau_r/\tau_{ro} = 0.86$) as illustrated by the insert in Fig. 5B.

For PI-0546 the shear stress reached a constant values of 151 MPa. For PI-0548, shear stress varied by <20 MPa with increasing shear strain. Small sinusoidal variations in shear stress, which are commonly observed in torsion experiments performed at a constant twist rate (Heidelbach et al., 2009; King et al., 2009, 2011a), arise because angular displacement is measured externally to the pressure vessel and is thus affected by friction on both the o-ring and the miter ring at the top of the sample assembly.

3.3. Texture and deformation

Texture and grain size of the olivine aggregates after shear deformation are illustrated in Fig. 6. Grain size reduction is ubiquitous, indicative of dynamic recrystallization. Despite small differences in finite shear strain and different shear strain rates, all sheared specimens show a similar final average grain size of 3–4 μm (Table 1). A few large grains (elongated porphyroclasts

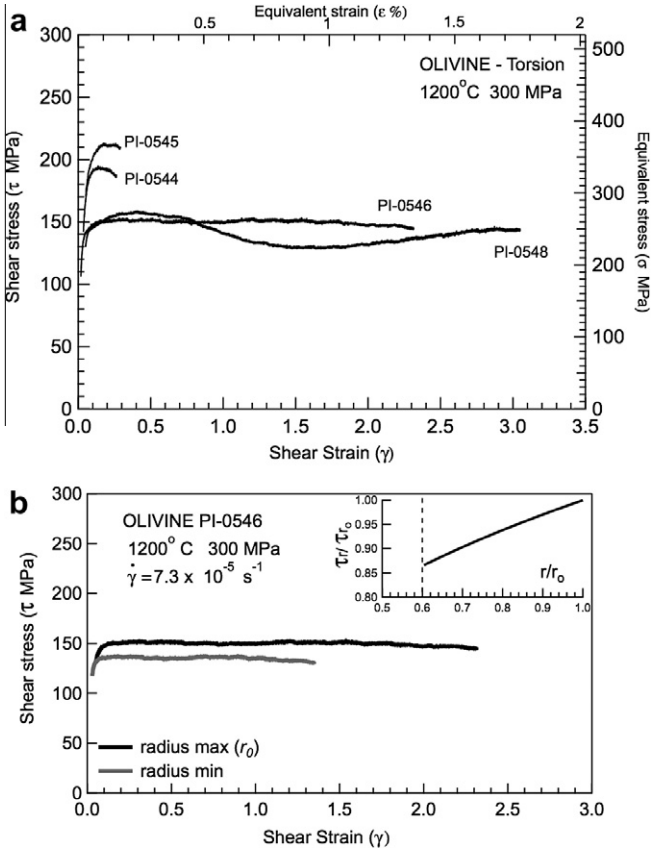

Fig. 5. (a) Plot of shear stress versus shear strain at constant twist rate for the fours torsion experiments at 1200 °C from this study. Axes are also shown for equivalent stress and equivalent strain (see details for stress and strain conversion in the main text). Shear stress drop due to slip at the sample boundary is not shown for PI-0544 and PI-0545, only steady state portions are shown. The full deformation curves are available in the online supplementary material (b) Shear stresses at the inner and outer surface of sample PI-0546 as a function of the shear strain. Insert in 5B shows the normalized shear stress as a function of the normalized radius demonstrating the low degree of heterogeneity in stress distribution within the polycrystalline hollow cylinder. The *dashed line* shows the limit of the central nickel capsule. The shear stress, τ, and radius, r, are normalized to the maximum values of shear stress, τ_0, and radius, r_0, respectively.

>30 μm long), which often contain numerous subgrain walls, have nevertheless survived to high shear strains. Again 120° triple junctions are still visible, although grain boundaries are often curved.

We constructed EBSD orientation maps of both axial and tangential sections for all deformed samples. However, because all samples display similar characteristics, we only present maps from one axial and one tangential section of sample PI-0548 in Fig. 7. In both maps, grains are colored according to their orientation relative to the shear direction (see inverse pole figure, at the bottom of Fig. 7). Blue, green or red shades indicate that the grains have their [100], [010] or [001] axes parallel to the shear direction, respectively. All maps obtained from the deformed samples (axial and tangential sections) have a dominantly blue shade indicating a [100] fabric (also called [100]-fiber or axial-[100]); this result suggests dominant activation of {0*kl*}[100] slip systems. Red shades are also frequently observed; they correspond to crystals oriented for dominant [001] slip. In the axial section presented in Fig. 7A, the colors are more varied close to the central Ni capsule and to the external Ni sleeve which indicates a more dispersed olivine CPO. The overall pattern is nevertheless similar in all sections. The maps on tangential sections, which records maximum shear strain is also characterized by dominant blue shades with frequent red shades as shown in Fig. 7B, indicating that most grains have [100], but a non-negligible fraction has [001] axes parallel to the shear direction even at high strains. Finally all deformed aggregates show a shape-preferred orientation of olivine grains marking a foliation and lineation; the observed obliquity between the foliation and the shear plane is consistent with the imposed dextral shear in Figs. 1C and 7B.

Pole figures illustrating the CPO of the different samples as a function of the finite shear strain are shown in Fig. 8a and b. They all exhibit the same pattern with [100] axes concentrated at low angle (PI-0544 and PI-0545) or parallel (PI-0546 and PI-0548) to the shear direction. The [010] axes are distributed in a girdle that is at high angle (nearly perpendicular) to the shear direction, with a moderately developed maximum at high angle to the shear plane. The [001] axes are more dispersed, forming a girdle normal to the lineation and a secondary weak maximum parallel to the lineation. The sample sheared to the highest finite shear strain (PI-0548) exhibits the strongest olivine CPO. Pole figures of the CPO for all axial sections and all tangential sections are given in Figs. S2 and S3, respectively (see online Supplementary material). Two movies showing the CPO evolution as a function of increasing strain in the axial sections of PI-0546 and PI-0548 are also provided in the online Supplementary material.

The evolutions of the average grain size, of the J-index for each crystallographic direction, and the global J-index (estimated from the ODF) as a function of the finite shear strain in sample PI-0546 are reported in Figs. 8b and 9. The J-index for both [100] and [010] axes increases as a function of strain, while the [001] axis J-index stays almost constant. However, toward the outer edge of the sample, the J-index (from ODF) increases rapidly with increasing strain (i.e., distance from the center of the sample) before decreasing abruptly very near the edge, as shown in Fig. 9.

The TEM observations of sheared sample PI-0546 in Fig. 10 reveal ubiquitous presence of free dislocations with [100] Burgers vectors as well as dislocations with [001] Burgers vectors (Fig. 10a). In addition to the free dislocations observed in Fig. 10, subgrain boundaries involving [100] dislocations and [001] dislocations are also present. No fluid inclusions were observed connected to dislocations or to grain boundaries.

3.4. Water content of deformed olivine

Unpolarized infrared spectra for samples PI-0546 and PI-0548 are presented in Fig. 4. Only the broad band (with still a large wavenumber range) attributed to inter-granular water-derived species (i.e., H_2O, OH^- and H^+) is still noticeably visible after deformation; even if the absorption coefficient is significantly smaller (i.e., area under the broad band decreased of 90%) than in the undeformed samples. However, the presence of the broad band undoubtedly indicates that the system was still hydrated, despite the lack of sharp peaks characteristic of O–H bonds stretching vibrations in the olivine structure. Thus quantification of water content within the olivine crystal structure (water *sensus stricto*) using the calibration of Paterson (1982) was not possible.

4. Discussion

4.1. Comparison with previous deformation experiments on olivine

The present results are compared with those from previous torsion and tri-axial compression experiments in Fig. 11. The hydrous olivine polycrystalline samples studied here are mechanically weaker (~30% weaker) than those previously deformed in torsion under dry conditions at the same temperature, confining pressure, and initial grain size by Bystricky et al. (2000). Another difference

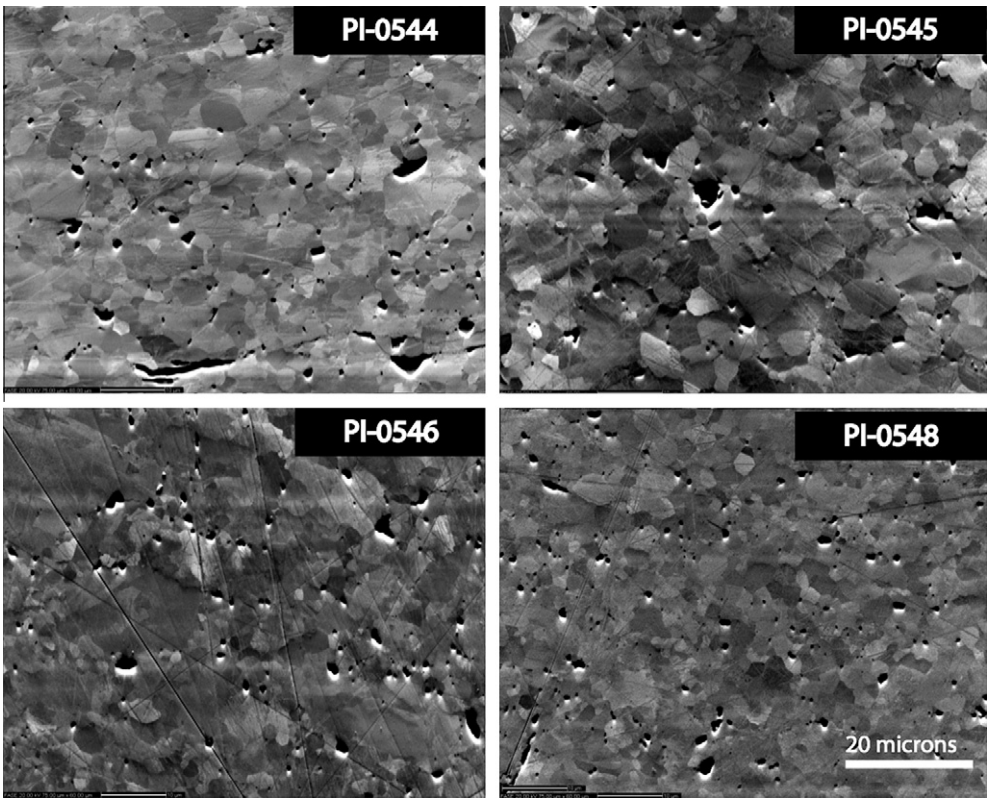

Fig. 6. Backscattered-electron images using SEM of the olivine aggregates after torsion showing grain size reduction. Dark areas are porosity and pluck out from polishing.

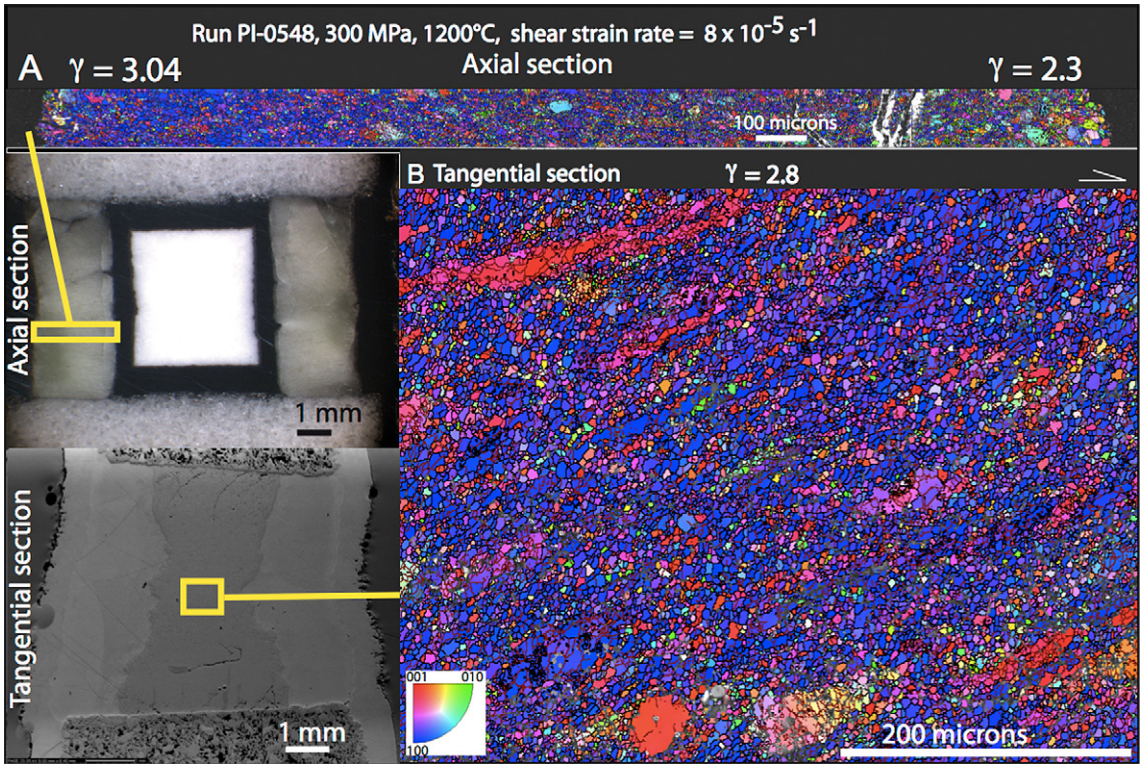

Fig. 7. EBSD maps from sample PI-0548 from the (a) axial section and (b) tangential sections. Map positions are given for both sections. Color scheme is indicated by inverse pole figure plotted with respect to the shear direction.

between the present data and those from Bystricky et al. (2000) is the absence of a stress peak followed by strain softening in our experiments. In the dry torsion experiments, a well-defined stress peak was observed at $0.07 < \gamma < 0.12$, which was followed by strain

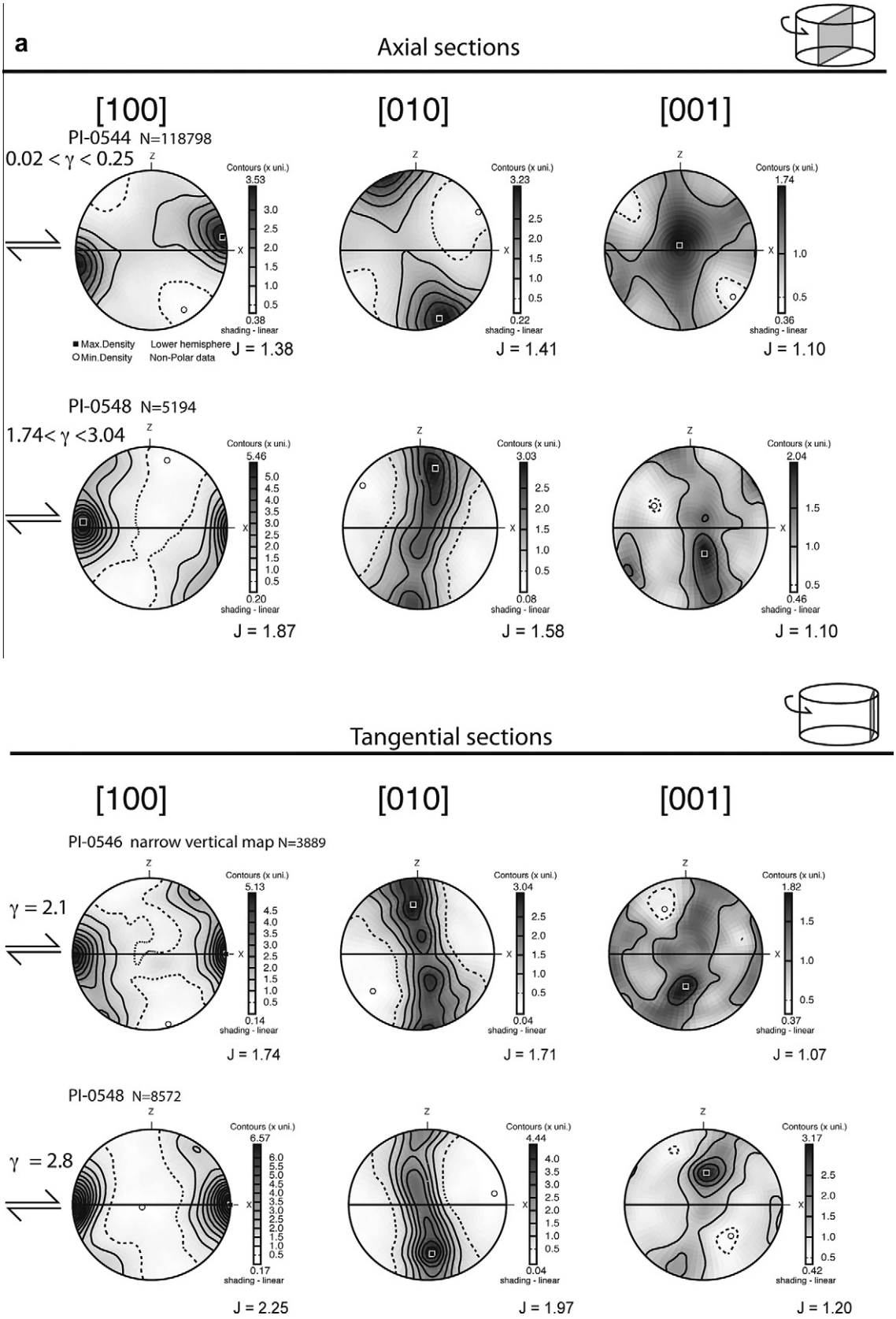

Fig. 8. (a) Pole figures showing the crystallographic preferred orientation of olivine aggregates in the axial and tangential sections after the shear experiments in a lower hemisphere equal-area projection. The shear direction is dextral. *N* is the number of analyzed olivine grains, maximum and minimum density contours are given at the top and bottom of the linear gray scale respectively. (b) Pole figures showing the crystallographic preferred orientation of olivine aggregates along the axial section for sample PI-0546 after the shearing. Projection is in a lower hemisphere with equal-area. The shear direction is dextral. N is the number of analyzed olivine grains, maximum and minimum density contours are given at the top and bottom of the linear gray scale respectively.

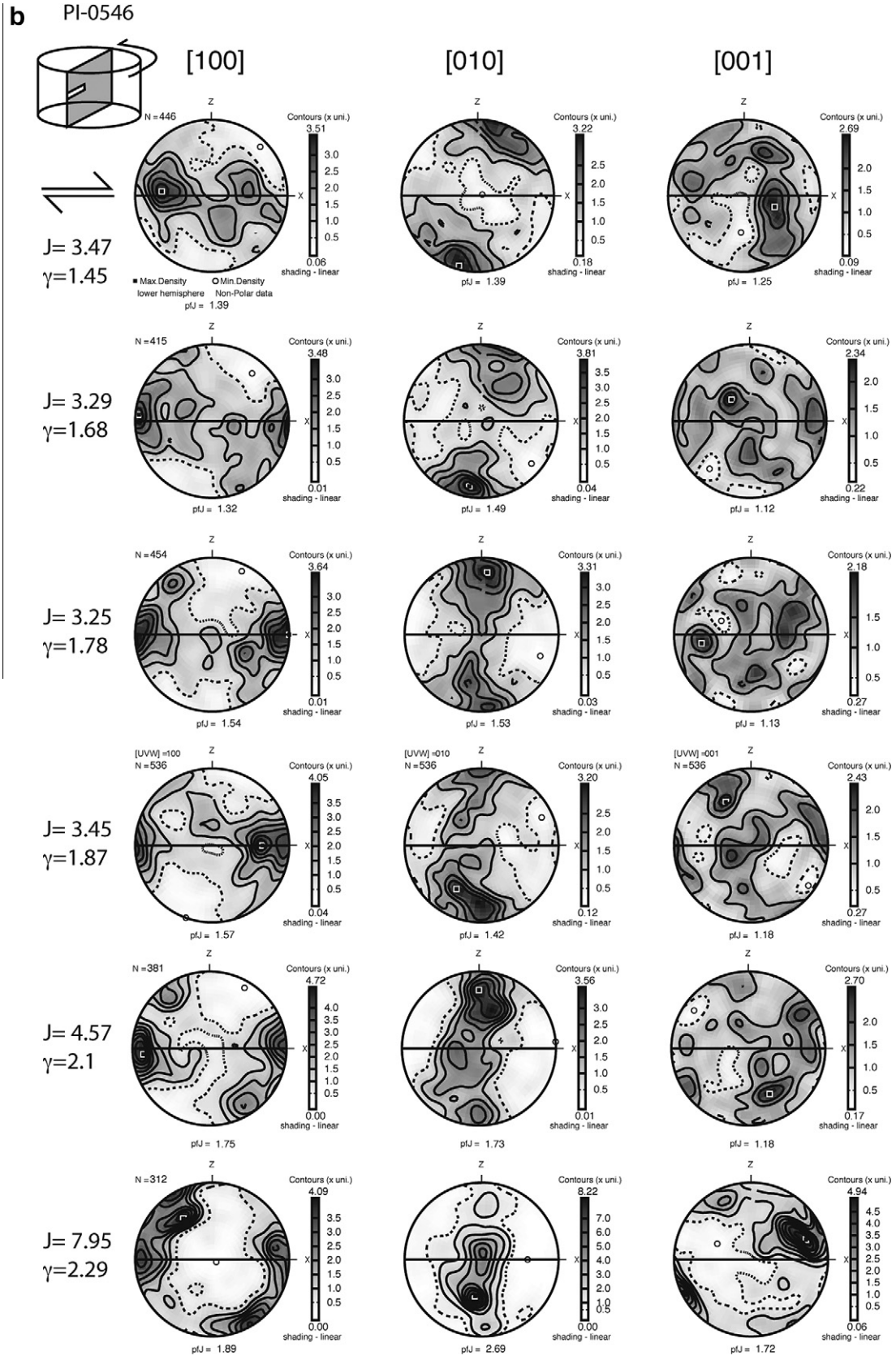

Fig. 8 (*continued*)

softening (Bystricky et al., 2000). In the present experiments, the magnitude of the stress drop is significantly smaller and the transition from the peak stress to the steady-state stress occurs over a much larger increment in strain.

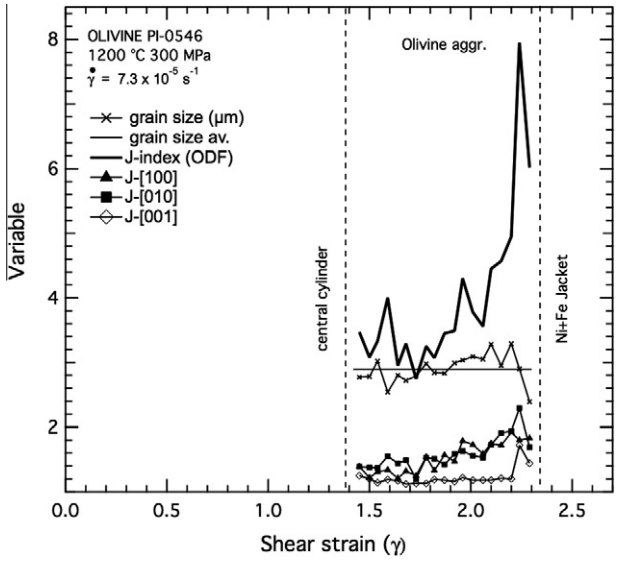

Fig. 9. Evolution of the grain size, J-index for each crystallographic axis, and total J-index (from ODF) as a function of shear strain based on 20 EBSD maps subsets from the axial sections of PI-0546. The *thin black line* indicates the average grain size for the entire axial section.

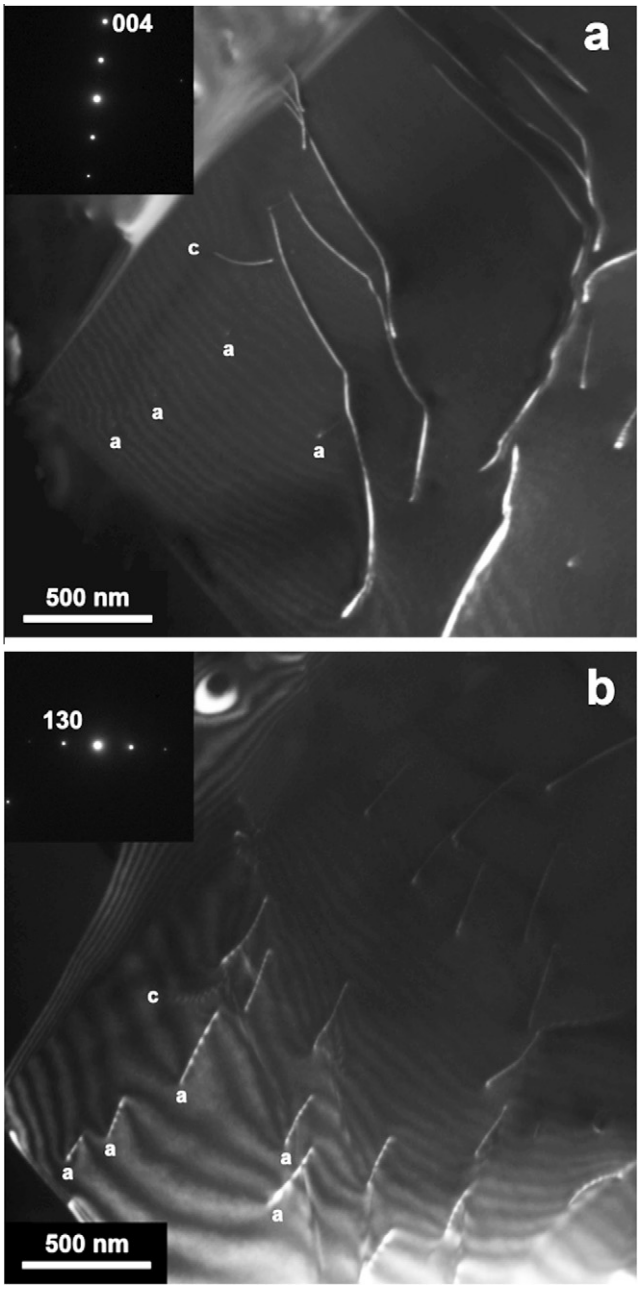

Fig. 10. Transmission electron microscopy. Characteristic deformation microstructure showing free dislocations in an olivine grain in sample PI-0546 (outer rim). (a) Weak-beam dark-field micrograph with g: 004. [001] dislocations are in contrast. [100] dislocations (labeled "a") leave a faint residual contrast where they reach the surface of the thin foil. (b) Same area as in (a), imaged in weak-beam dark-field with g: 130. Only [100] dislocations are in contrast. [001] dislocations (labeled "c") are out of contrast.

The original creep test results from Mei and Kohlstedt (2000) at 1200 °C and the flow law (constitutive equation, Eq. (1)) for creep of olivine under hydrous conditions at 300 MPa derived by Hirth and Kohlstedt (2003), based on the dataset from Mei and Kohlstedt (2000) were also included in Fig. 11. The mechanical behavior of our samples is consistent with these hydrous flow laws, confirming that our aggregates were undersaturated in water, but not fully dry ($\sim$5 ppm wt. H_2O) as suggested from FTIR measurements.

CPO patterns for our wet olivine aggregates have a roughly axial symmetry around the maximum concentration of [100]. They are thus similar to the CPO obtained by Bystricky et al. (2000) for dry polycrystalline olivine ($\ll$1 ppm wt. H_2O) for the same shear strain ($\gamma \approx 3$). Our CPOs are however weaker. Weaker CPO for similar finite strains may result from either more effective dynamic crystallization (e.g., Falus et al., 2011) or from accommodation of a significant part of the deformation by processes other than dislocation glide (e.g., Casey et al., 1998; Hirth and Kohlstedt, 2003; Le Roux et al. 2008; Soustelle et al. 2009).

Reporting our data and the results from Bystricky et al. (2000) in the olivine 'fabric classification' diagram proposed by Karato (2008) indicates that the field of 'D-type' fabrics should be extended to significantly lower shear stresses and to higher water contents, up to 212 ppm H/Si (i.e., 212 ppm H/Si equals 13 ppm wt. H_2O), if the initial water content is used; Fig. 12. An important point that one has to keep in mind when examining this 'fabric classification' diagram is the level of uncertainty in both water content (at least ±30% when using the calibration of Paterson (1982), see Demouchy (2010a) for an example) and differential stress (±10–15% based on measurements of dislocation densities, see Jung and Karato, 2001b). If uncertainties for water contents and stresses are integrated in the 'fabric classification' diagram, the different fields still exist, but overlap significantly. In addition, Karato and co-workers only presented one FTIR spectrum for a C-type fabric (Jung et al., 2006), thus strongly limiting constraints on the water speciation in their fine-grained olivine aggregates. Finally, the effect of pressure, which may be very important in determining the dominant slip systems and thus the resultant fabric (Couvy et al., 2004; Jung et al., 2009; Karato et al., 2008), is not considered in this diagram. The present experiments were performed at significantly lower pressure (300 MPa) than the data set originally used to construct the diagram (1.5–2 GPa).

The axial-[100] or 'D-type' olivine CPOs produced in our experiments (Fig. 8a and b) are consistent with dominant activation of {0*kl*}[100] slip systems, with (010)[100] predominating. TEM observations show, however, that both [100] and [001] Burgers vectors are ubiquitously present in olivine grains, suggesting that [001] glide was also active. Development of D-type fabrics in olivine by activation of multiple glide systems is in agreement with CPO development in viscoelastic self-consistent simulations (Tommasi et al. 2000). In these simulations, glide on (010)[100]

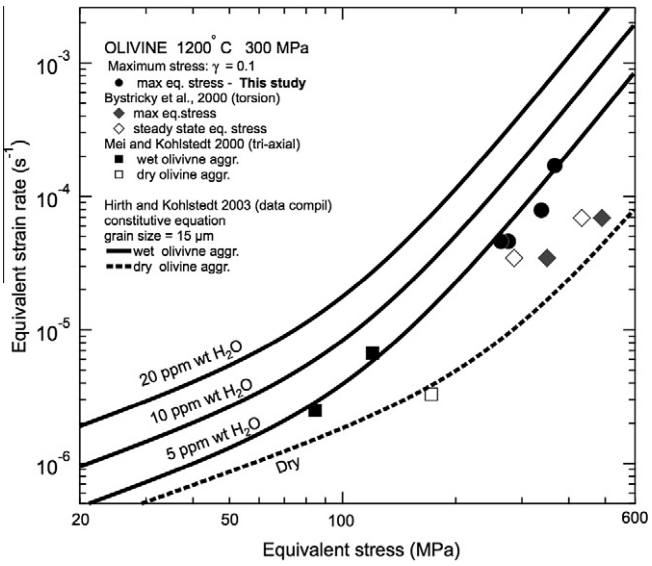

Fig. 11. Equivalent strain rate versus equivalent stress at 1200 °C for all experiments in this study. *Dots* are from this study. *Black* and *white diamonds* are for maximum stress and steady state stress, respectively from the torsion experiments on dry olivine by Bystricky et al. (2000). The *white* and *black squares* are from Mei and Kohlstedt (2000) for dry and water-rich olivine aggregates, respectively. Flow laws (constitutive equations) for olivine creep under hydrous (*dark lines are* shown for various constant water content) and dry (*dashed line*) conditions from Hirth and Kohlstedt (2003) is also shown for comparison. For the diffusion creep part of the constitutive equation, grain size was fixed to 15 μm.

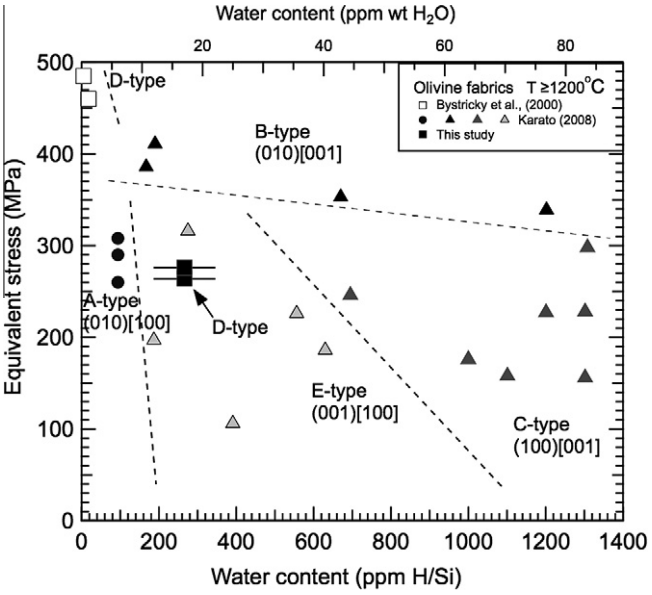

Fig. 12. Deformation fabrics of olivine at high temperature ($T \geqslant 1200$ °C) as a function of the water content as proposed by Karato (2008). All water contents are given following the calibration of Paterson (1982). Only initial water content (13 ppm wt. H_2O) ppm for sample PI0546 and PI-0548 are reported in the diagram, although mechanical data suggested 5 ppm wt. H_2O during the experiments. See text for comments on fabric domain definitions and accuracy. *NB*: For olivine Fo_{90}, 1 ppm wt. H_2O = 16.32 H/10^6 Si.

accommodates most of the deformation, but glide on {*hk*0}[001] systems may contribute to up to 30% of the total strain at the aggregate scale, depending on the texture and on the imposed strain compatibility constraints. This systematic activation of multiple slip systems implies that the transitions between different CPO 'types' are continuous. This argument is consistent with observations in naturally deformed mantle rocks, which show continuous gradations between A-, D-, and E-type fabrics (Tommasi et al. 2000; Mainprice 2000).

4.2. Water speciation and water-weakening in fine-grained olivine aggregates at high temperature and low pressure

The infrared spectra from our samples (Fig. 4) have identical features to those observed in many other studies on water-weakening in olivine aggregates (Chopra and Paterson, 1984; Karato et al., 1986; Mei and Kohlstedt, 2000; Zimmerman and Kohlstedt, 2004; Faul and Jackson, 2007; Aizawa et al., 2008), where a broad band associated with inter-granular hydrous component masks most of the signal produced by OH^- bonds in the olivine structure. This broad band hinders a precise analysis of water speciation and quantification of H content in fine-grained olivine aggregates. Our infrared analyses confirm therefore that the olivine aggregate contains 'water' *sensus lato* (i.e., water-derived species in the system) both before and after the torsion experiments with a speciation of water-derived species (inter-granular H_2O and OH^-) in the pores and/or grain boundaries, but do not provide firm evidence of 'water' *sensus stricto* (i.e., hydrogen in olivine embedded as point defects) in the olivine structure of the deformed samples (Fig. 4).

We propose two possible explanations for the absence of sharp FTIR peaks related to OH^- in our deformed olivine. First, partial dehydration of the aggregate would be consistent with the small amount of hardening observed in run PI-0548, which had the longest duration (~9 h, Table 1) and the convergence of our low strain rate data toward the steady state results obtained under anhydrous conditions by Bystricky et al. (2000). Second, the quench rate of 60°/min might be too slow, permitting partial dehydration of the olivine crystals during the quench. Thus, it will leave the post-mortem olivine structure dry while preserving only some water-derived species within inter-granular pores and grain boundaries (below their saturation level). Because H diffusion along grain boundaries is almost four orders of magnitude faster than through the olivine grains, (i.e., $D_H^{gb} = 5 \times 10^{-6}\ m^2 s^{-1}$ at 1200 °C in grain boundaries, Demouchy 2010a; whereas $D_H^{pp} = 1 \times 10^{-9}\ m^2 s^{-1}$ and $D_H^{pv} = 2.77 \times 10^{-11}\ m^2 s^{-1}$ in the olivine structure at 1200 °C for the proton-polaron and proton-vacancy mechanisms, respectively, Demouchy and Mackwell, 2006), and that the sample is very fine grained (<10 μm), thus H flux along grain boundaries will be an effective dehydration path during simultaneous cooling and decompression of the polycrystal. For instance, in a strongly water-undersaturated system, a grain of 20 μm in diameter will dehydrate in ~1 s at 1200 °C and low pressure. Alternatively, during torsion at high pressure and temperature, water-derived species in the pores and/or within grain boundaries could also diffuse very rapidly at short scale toward the olivine crystal, ensuring a streaming of H. As a consequence, we consider that the olivine polycrystal must have been 'wet' *sensus lato* during the torsion, even if the OH^- content within the olivine grains after the experiments cannot be accurately quantified with FTIR. We must point out that even the use of a synchrotron IR beam with a spot size <10 μm or a nuclear probe (e.g., Bureau et al., 2003, 2009) would not permit an accurate detection and quantification of OH^- in olivine because the grains are basically not thick enough and the concentration level too low.

In conclusion, although the mechanical data show a clear weakening relative to data on dry olivine polycrystals (by 30%), we cannot relate this weakening to any robust measurement of OH^- in the olivine structure. By consequence, we suggest that water-weakening in fine-grained olivine aggregates involves the participation not only of point defects (i.e., Si vacancies, which enhance the dislocation climb velocity, Kohlstedt, 2006), but also of linear and planar defects, with water-derived species in grain boundaries

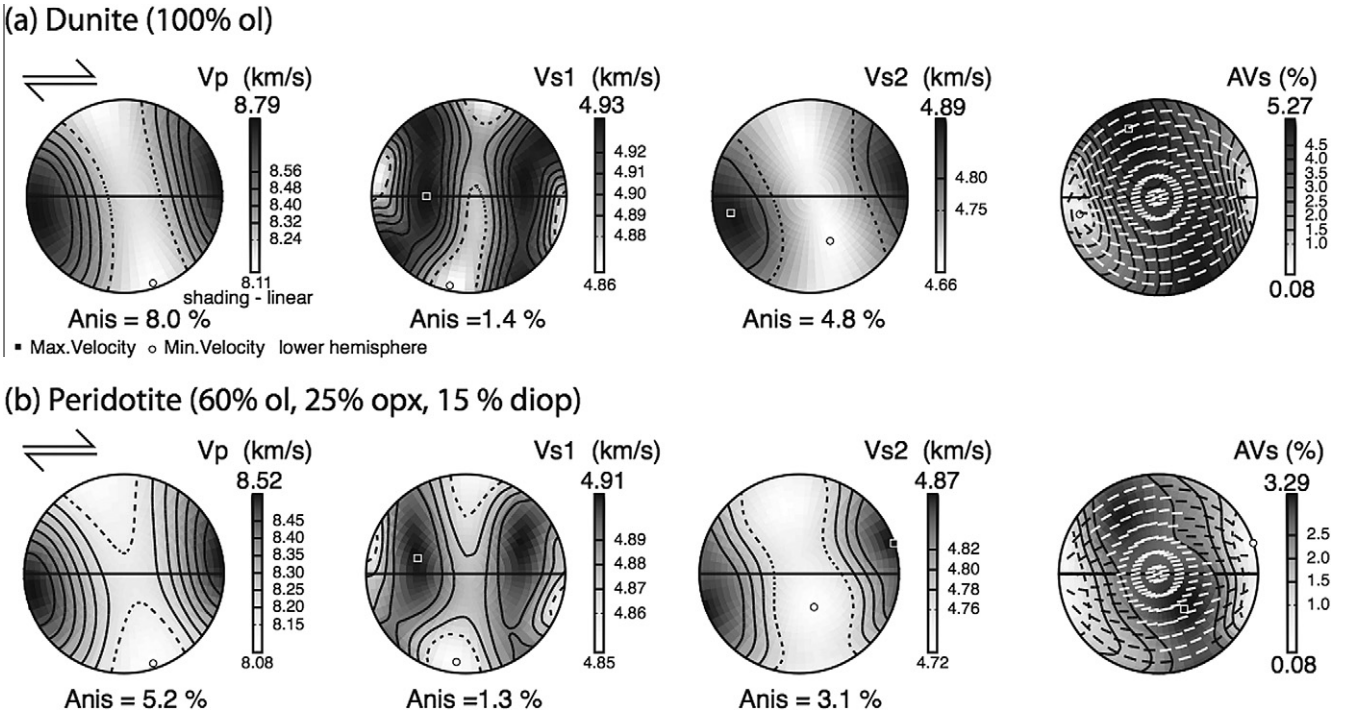

Fig. 13. Modeled three-dimensional compression and shear waves velocity distribution (Vp and $Vs_{(1-2)}$, respectively) as well as polarization anisotropy (AVs, plotted together with VS1 polarization) for (a) sheared dunite (100% olivine), and (b) sheared peridotite with a 'pristine' mantle modal composition (60% olivine, 25% orthopyroxene, 15% diopside). Voigt–Reuss–Hill averages plotted in a lower hemisphere equal-area projection. *Solid line* marks the shear plane. *Arrows* in the upper left corner indicates the shear direction (dextral). Elastic constants used for these models are given in Table 2.

playing an important role. For coarse-grained olivine-rich rocks, with grain sizes >1 mm, as commonly observed in mantle-derived peridotite xenoliths and massifs, we may expect that water-derived species in grain boundaries will have a less important contribution to the rheology of the system (Demouchy 2010a). However the water-weakening processes in coarse-grained peridotites still remain to be characterized and quantified.

4.3. Shear zones in the lithospheric mantle

Mantle rocks deformed at high temperature commonly exhibit coarse-grained microstructures and a well-defined olivine CPO with [100] axes parallel to crystals' elongation (when the latter is present); J-indexes in these rocks range from 2 to 20 with a peak between 8 and 10 (Ben Ismail and Mainprice, 1998; Tommasi et al. 2000). Localization of deformation producing mylonites and ultramylonites is limited to low temperature conditions (900–1000 °C) and is accompanied by intensive dynamic recrystallization, which results in weak olivine CPO as indicated by J-indexes below five (e.g., Newman et al., 1999; Dijkstra et al., 2004; Michibayashi and Mainprice, 2004; Vauchez et al., 2012; Kaczmarek and Tommasi, 2011; Falus et al., 2011).

Although finer-grained, our experimentally sheared olivine aggregates display deformation textures similar to those observed in mylonites from Oman (Michibayashi and Mainprice, 2004) and Lanzo (Kaczmarek and Tommasi, 2011) as well as in xenoliths from the Carpathians (Falus et al., 2011). They show elongated porphyroclasts with core-and-mantle structures enclosed in a fine-grained matrix composed of roughly equiaxed recrystallized grains, which may also contain a few subgrain walls (Fig. 7). J-indexes are also similar, averaging around 3–5 and reaching 7 in the most deformed domains (Fig. 9). The water content in olivine from natural mylonitic peridotites is rarely quantified, due to the small grain sizes (<30 μm). Nevertheless 'hydrous' peridotite mylonites containing oriented amphiboles and/or chlorite do exist, indicating synkinematic percolation of hydrous, potentially supersaturated, fluid/melt may be an essential process for the deformation of the lithospheric mantle under low-temperatures conditions (Vissers et al. 1987; Dijkstra et al., 2004).

Table 2
Elastic stiffness coefficients C_{ij} (in GPa) calculated for (A) a dunite (with 100% olivine) and (B) an aggregate of 'pristine' mantle (60% olivine, 25% orthopyroxene, 15% diopside).

J	*i*					
	1	2	3	4	5	6
(A)						
1	223.41	77.24	76.71	−0.1	−0.35	−4.69
2	77.24	257.23	77.27	−2.75	0.23	−3.6
3	76.71	77.27	224.48	−1.79	0.37	−0.39
4	−0.1	−2.75	−1.79	79.58	−1.47	0.05
5	−0.35	0.23	0.37	−1.47	73.49	−0.81
6	−4.69	−3.6	−0.39	0.05	−0.81	76.76
(B)						
1	217.76	69.93	70.50	−0.42	−0.03	−2.76
2	69.93	238.89	70.41	−0.88	0.57	−2.10
3	70.50	70.41	220.04	−0.66	0.36	−0.39
4	−0.42	−0.88	−0.66	76.33	−0.86	0.13
5	−0.3	0.57	0.36	−0.86	74.34	−0.50
6	−2.76	−2.10	−0.39	0.13	−0.50	77.70

4.4. Consequences for seismic anisotropy

The three-dimensional distribution of seismic velocities in a polycrystalline aggregate can be estimated by averaging the individual grain elastic tensors as a function of the crystallographic orientations and mineralogical composition of the aggregate (Mainprice and Humbert, 1994). The seismic properties of the sheared aggregate with the strongest CPO (Fig. 8) calculated for a

pressure of 0.3 GPa and 1200 °C are presented in Fig. 13. To illustrate the anisotropy dilution due to occurrence of other mineral phases, we also present the seismic properties of a lherzolite (60% olivine, 25% orthopyroxene, and 15% diopside) with the same olivine CPO as the experimental sample and orthopyroxene and diopside CPO measured in naturally deformed peridotites (A. Tommasi, unpublished data) and oriented as expected if all minerals were experiencing to the same deformation. The rock elastic constants for both cases are given in Table 2.

P- and slow S-wave propagations are faster at low angle from the shear direction, and slower normal to the shear plane. Fast S-waves are always polarized parallel to the shear direction and polarization anisotropy is minimum for waves propagating at low angle to the shear direction (Fig. 13). As expected (e.g., Mainprice and Silver, 1993), the azimuthal anisotropies for both P- and S-waves and the S-wave polarization anisotropy are slightly reduced in the lherzolite. These calculations predict therefore a moderate seismic anisotropy within a slightly hydrated mantle shear zone.

5. Conclusion

Results from shear deformation experiments on aggregates of iron-bearing olivine (Fo_{90}) under hydrous conditions suggest a relatively minor weakening (less than one order of magnitude) due to the presence of water-derived species in the system, with most of the water contained in pores and/or grain boundaries. Deformed samples exhibit CPOs characterized by concentrations of [100] and (010) subparallel to the shear direction and shear plane, respectively. In addition, dispersion of [010] and [001] axes in a girdle at high angle to the lineation indicates activation of other {0*kl*}[100] systems (axial-[100] or 'D-type' fabric, Karato, 2008). The TEM observations of a high strain domain ($\gamma > 1$) in the deformed samples show both [100] and [001] dislocations, indicating that [001] glide is also active, consistently with CPO evolution in viscoplastic self-consistent models where A- and D-type fabrics develop by activation of multiple slip systems with a more or less marked predominance of (010)[100]. One has to note however that the low water fugacity achievable at 300 MPa of confining pressure hinders a thorough investigation of this transition. Nevertheless, our results show that at low pressures, the field of 'D-type' fabrics, which results from olivine deformation with dominant activation of the {0*kl*}[100] systems, should be extended to lower stresses and higher water contents. Extrapolation of the present experimental results to the shallow upper mantle in subduction zones and to trans-lithospheric faults and shear zones implies that the presence of moderate amounts of water *sensus lato* in mantle rocks produces weakening, but does not change the dominant glide systems in olivine or its seismic anisotropy.

Acknowledgments

SD was supported by the EU FP7 "PoEM" project (Marie Curie fellowship FP7-IRG-230748). The deformation experiments were performed at the Dept. Geology and Geophysics, University of Minnesota (USA), where the deformation laboratory was supported by NSF grants EAR-0910687 and EAR-1015343. This manuscript has greatly benefited from informal reviews by D.L. Kohlstedt, M.E. Zimmermann and L.N. Hansen. SD is deeply grateful to A. Vauchez and V. Soustelle for useful discussions, as well as to M.E. Zimmermann, L.N. Hansen, A.C Withers and A. Dillman for excellent technical, logistical and prompt help in the lab in Minneapolis. C. Nevado and D. Delmas are thanked for providing high-quality polishing of sections for SEM-EBSD and FTIR measurements. The FTIR analyses were performed together with D. Maurin at the Lab. Colloids, Verre et Nanomateriaux, at Université Montpellier 2 (France). The TEM and EBSD-SEM national facilities in Lille and Montpellier, respectively, are supported by the Institut National de Sciences de l'Univers (INSU) du Centre National de la Recherche Scientifique (CNRS, France). The EBSD-SEM facility in Montpellier and TEM facility in Lille are also supported by the Conseil Régional Languedoc-Roussillon (France) and by the Conseil Régional du Nord-Pas de Calais, (France), respectively.

References

Aines, R.D., Rossman, G.R., 1984. Water in minerals? A peak in the infrared. J. Geophys. Res. 89 (B6), 4059–4071.
Aizawa, Y., Barnhoorn, A., Faul, U.H., Fitz Gerald, J.D., Jackson, I., Kovacs, I., 2008. Seismic properties of Anita Bay dunite: an Exploratory Study of the influence of water. J. Petrol. 49 (4), 841–855.
Bai, Q., Kohlstedt, D.L., 1992. High-temperature creep of olivine single crystals, 2. dislocation structures. Tectonophysics 206, 1–29.
Barnhoorn, A., Bystricky, M., Burlini, L., Kunze, K., 2004. Post-deformational annealing of calcite rocks. Tectonophysics 403 (1–4), 167–191.
Barnhoorn, A., Bystricky, M., Kunze, K., Burlini, L., Burg, J.-P., 2005. Strain localization in bimineralic rocks: experiment deformation of synthetic calcite-anhydrite aggregates. Earth Planet. Sci. Lett. 240, 748–763.
Bell, D., Rossman, G., Maldener, J., Endisch, D., Rauch, F., 2003. Hydroxide in olivine: a quantitative determination of the absolute amount and calibration of the IR spectrum. J. Geophys. Res. 108 (B2).
Ben Ismail, W., Mainprice, D., 1998. An olivine fabric database: an overview of upper mantle fabrics and seismic anisotropy. Tectonophysics 296, 145–157.
Bolfan-Casanova, N., Keppler, H., Rubie, D., 2000. Water partitioning between nominally anhydrous minerals in the $MgO–SiO_2–H_2O$ system up to 24 GPa: implications for the distribution of water in the Earth's mantle. Earth Planet. Sci. Lett. 182, 209–221.
Bunge, H.J., 1982. Texture Analysis in Materials Sciences. Butterworth, London.
Bureau, H., Trocellier, P., Shaw, C., Khodja, H., Bolfan-Casanova, N., Demouchy, S., 2003. Determination of the concentration of water dissolved in glasses and minerals using nuclear microprobe. Nucl. Instrum. Meth. Phys. Res. B 210, 449–454.
Bureau, H., Reapsaet, C., Khodja, H., Heidelbach, F., Carraro, Aubaud, C., 2009. Determination of hydrogen content in geological samples using Elastic Recoil Detection Analysis (ERDA). Geochim. Cosmochim. Acta 73, 3311–3322.
Bystricky, M., Heidelbach, F., Mackwell, S.J., 2006. Large-strain deformation and strain partitioning in polyphase rocks: dislocation creep of olivine-magnesiowustite aggregates. Tectonophysics 427, 115–132.
Bystricky, M., Kuntze, K., Burlini, L., Burg, J.-P., 2000. High shear strain of olivine aggregates: rheological and seismic consequences. Science 290, 1564–1567.
Casey, M., Kunze, K., Olgaard, D.L., 1998. Texture of Solnhofen limestone deformed to high strains in torsion. J. Struct. Geol. 20, 255–267.
Chen, S., Hiraga, T., Kohlstedt, D.L., 2006. Water weakening of clinopyroxene in the dislocation creep regime. J. Geophys. Res.. http://dx.doi.org/10.1029/2005JB003885.
Chopra, P.N., Paterson, M.S., 1984. The role of water in the deformation of dunite. J. Geophys. Res. 89, 7861–7876.
Couvy, H., Frost, D.J., Heidelbach, F., Nyilas, K., Ungar, T., Mackwell, S.J., Cordier, P., 2004. Shear Deformation experiments of forsterite at 11 GPa – 1400 °C in the multianvil apparatus. Eur. J. Mineral. 16, 877–889.
Delle Piane, C., Burlini, L., Kunze, K., Brack, P., Burg, J.-P., 2008. Rheology of dolomite: large strain torsion experiments and natural examples. J. Struct. Geol. 30, 767–776.
Demouchy, S., 2010a. Diffusion of hydrogen in olivine grain boundaries and implications for the survival of water-rich zones in the Earth's mantle. Earth Planet. Sci. Lett. 295, 305–313.
Demouchy, S., 2010b. Hydrogen diffusion in spinel grain boundaries and consequences for chemical homogenization in hydrous peridotite. Contrib. Mineral. Petrol. 160, 887–898.
Demouchy, S., Mackwell, S., 2006. Mechanisms of hydrogen incorporation and diffusion in iron-bearing olivine. Phys. Chem. Minerals 33, 347–355.
Demouchy, S., Mainprice, D., Tommasi, A., Couvy, H., Barou, F., Frost, D.J., Cordier, P., 2011. Forsterite to wadsleyite phase transformation under shear stress and consequences for the Earth's mantle transition zone. Phys. Earth Planet. Int. 184, 91–104.
Demouchy, S., Schneider, S.E., Mackwell, S.J., Zimmerman, M.E., Kohlstedt, D.L., 2009. Experimental deformation of olivine single crystal at lithospheric temperature. Geophys. Res. Lett. 36, L04304.
Dijkstra, A.H., Drury, M.R., Visser, R.L.M., Newman, J., Van Roermund, H.L.M., 2004. Shear zone in the upper mantle: evidence from alpine- and ophiolite-type peridotite massifs. In: Alsop, G., Holdsworth, R.E., McCaffrey, K.J., Hand, M.

(Eds.), 2004, Flow Processes in Faults and Shear Zones. Geological Society of London, Special Pub., London.
Etheridge, M.A., Wilkie, J.C., 1981. An assessment of dynamically recrystallized grain size as a paleopiezometer in quartz-bearing mylonite zone. Tectonophysics 78, 475–508.
Falus, G., Tommasi, A., Soustelle, V., 2011. The effect of dynamic recrystallization on olivine crystal preferred orientations in mantle xenoliths deformed under varied stress conditions. J. Struct. Geol. 33, 1528–1540.
Faul, U.H., Jackson, I., 2007. Diffusion creep of dry, melt-free olivine. J. Geophys. Res. 112. http://dx.doi.org/10.1029/2006JB004586.
Frost, H.J., Ashby, M.F., 1982. Deformation Mechanism Maps: The Plasticity and Creep of Metals and Ceramics. Pergamon Press, Oxford (p. 166).
Hansen, L.N., Zimmerman, M.E., Kohlstedt, D.L., 2011. Grain boundary sliding in San Carlos olivine: flow law parameters and crystallographic-preferred orientation. J. Geophys. Res. 116. http://dx.doi.org/10.1029/2011JB008220.
Heidelbach, F., Stretton, I., Langenhorst, F., Mackwell, S.J., 2003. Fabric evolution during high shear strain deformation of magnesiowustite (Mg0.8Fe0.2)O. J. Geophys. Res. 108 (B3) (doi:10.1029/2001JB001632).
Heidelbach, F., Terry, M.P., Bystricky, M., Holzapfel, C., McCammon, C., 2009. A simultaneous deformation and diffusion experiments: quantification of the role of deformation in enhancing metamorphic reactions. Earth Planet. Sci. Lett. 278 (3–4), 386–394.
Hirose, T., Bystricky, M., Kunze, K., Stunitz, H., 2006. Semi-brittle flow during dehydration of lizardite-chrysotile serpentinite deformed in torsion: implication for the rheology of oceanic lithosphere. Earth Planet. Sci. Lett. 249, 484–493.
Hirth, G., Kohlstedt, D.L., 2003. Rheology of the upper mantle and the mantle wedge: a view from the experimentalists. In: Eiler, J. (Ed.), Inside the subduction factory, Geophysical Monograph 138. American Geophysical Union, Washington DC, pp. 83–105.
Jung, H., Karato, S.-I., 2001a. Water-induced fabric transitions in olivine. Science 293, 1460–1463.
Jung, H., Karato, S.-I., 2001b. Effect of water on dynamically recrystallized grain-size of olivine. J. Struct. Geol. 23, 1337–1344.
Jung, H., Katayama, I., Jiang, Z., Hiraga, T., Karato, S.-I., 2006. Effect of water and stress on the lattice-preferred orientation of olivine. Tectonophysics 421, 1–22.
Jung, H., Mo, W., Green, H.W., 2009. Upper mantle seismic anisotropy resulting from pressure-induced slip transition in olivine. Nature Geosciences 2, 73–77.
Kaczmarek, M.-A., Tommasi, A., 2011. Anatomy of an extensional shear zone in the mantle, Lanzo massif. Italy. Geochem. Geophys. Geosyst 12. http://dx.doi.org/10/1029/2011GC0033627.
Karato, S.I., Paterson, M.S., Fitzgerald, J.D., 1986. Rheology of synthetic olivine aggregates: influence of grain size and water. J. Geophys. Res. 91, 8151–8176.
Karato, S.-I., 1990. Grain growth kinetics in olivine aggregats. Tectonophysics 168, 255–273.
Karato, S., 2008. Deformation of Earth Materials: An Introduction to the Rheology of Solid Earth. Cambridge University Press.
Karato, S.-I., Jung, H., Katayama, I., Skemer, P., 2008. Geodynamic significance of seismic anisotropy of the upper mantle: new insights from laboratory studies. Annu. Rev. Earth Planet. Sci. 36, 59–95.
Kawazoe, T., Karato, S.-I., Otsuka, K., Jing, Z., Mookerjee, M., 2008. Shear deformation of dry polycrystalline olivine under deep upper mantle conditions using rotational Drickamer apparatus (RDA). Phys. Earth Planet. Int. 174 (1–4), 128–137.
Keefner, J.W., Mackwell, S.J., Kohlstedt, D.L., Heidelbach, F., 2011. Dependence of the creep of dunite on oxygen fugacity: implications for viscosity variations in Earth's mantle. J. Geophys. Res. 16. http://dx.doi.org/10.1029/2010JB007748.
Keppler, H., Rauch, M., 2000. Water solubility in nominally anhydrous minerals measured by FTIR and ^{1}H MAS NMR: effect of sample preparation. Phys. Chem. Minerals 27, 371–376.
King, D.S.H., Zimmerman, M.E., Kohlstedt, D.L., 2009. Stress-driven melt segregation in partially molten olivine-rich rocks deformed in torsion. J. Petrol. 51 (1–2), 21–42.
King, D.S.H., Holtzman, B.K., Kohlstedt, D.L., 2011a. An experimental investigation of the interactions between reaction-driven and stress-driven melt segregation. 1. Application to mantle melt extraction. Geochem. Geophys. Geosys. (http://dx.doi.org/10.1029/2011GC003684).
King, D.S.H., Holtzman, B.K., Kohlstedt, D.L., 2011b. An experimental investigation of the interactions between reaction-driven and stress-driven melt segregation. 2. Disaggregation at high melt fraction. Geochem. Geophys. Geosys. (http://dx.doi.org/10.1029/2011GC003685).
Kohlstedt, D.L., 2006. The role of water in high-temperature rock deformation. In: Keppler, H., Smyth, J.R. (Eds.), Review in Mineralogy, vol. 62. Water in NAMs, MSA.
Kohlstedt, D.L., 2007. Constitutive equations, rheological behavior, and viscosity of rocks. In: Schubert, G. (Ed.), Treatise in Geophysics, 2: Minerals Physics. Elsevier.
Kohlstedt, D.L., Zimmerman, M.E., Mackwell, S.J., 2010. Stress-driven melt segregation in partially molten feldspathic rocks. J. Petrol. 52, 9–19. http://dx.doi.org/10.1093/petrology/egp043.
Larkin, L., Zimmerman, M.E., Kohlstedt, D.L., 2005. Phase separation during deformation of a two-phase rock. Eos. Trans. AGU, 86(52) Fall Meet Suppl Abs T41C–1320.
Le Roux, V., Tommasi, A., Vauchez, A., 2008. Feedbacks between melt percolation and deformation in an exhumed lithosphere-asthenosphere boundary. Earth Planet. Sci. Lett. 274, 401–413.
Mackwell, S.J., 2008. Rheological Consequences of Redox State. In: MacPherson, G.J., (Ed.), Oxygen in the solar system. In: Rosso, J.J., (Ed.), vol. 68. Mineralogical Society of America, Chantilly (Virginia), pp. 55–569.
Mackwell, S.J., Kohlstedt, D.L., Paterson, M.S., 1985. The role of water in the deformation of olivine single crystals. J. Geophys. Res. 90 (B13), 11319–11333.
Mainprice, D., 2000. The estimation of seismic properties of rocks with heterogeneous microstructures using a local cluster model - Preliminary results. Phys. Chem. Earth (A) 25, 155–161.
Mainprice, D., Humbert, M., 1994. Methods of calculation petrophysical properties from lattice preferred orientation data. Surv. Geophysics 15, 575–592.
Mainprice, D., Silver, P.G., 1993. Interpretation of SKS-waves using samples from the subcontinental lithosphere. Phys. Earth Planet. Inter. 78, 257–280.
Mei, S., Kohlstedt, D.L., Harlow, G.E., 2000. Influence of water on plastic deformation of olivine aggregates 2. Dislocation creep regime. J. Geophys. Res. 105 (B9), 21471–21481.
Miller, G.H., Rossman, G.R., Harlow, G.E., 1987. The natural occurrence of hydroxide in olivine. Phys. Chem. Minerals 14, 461–472.
Michibayashi, K., Mainprice, D., 2004. The role of pre-existing mechanical anisotropy on shear zone development within oceanic mantle lithosphere: an example from the Oman ophiolite. J. Petrol. 45, 404–414.
Mosenfelder, J.L. et al., 2011. Analysis of hydrogen in olivine by SIMS: evaluation of standards and protocol. Am. Min. 96, 1725–1741 (AGU monograph volume).
Newman, J., Lamb, W.M., Drury, M.R., Vissers, R.L.M., 1999. Deformation processes in a peridotite shear zone: reaction-softening by an H_2O-deficient, continuous net transfer reaction. Tectonophysics 303, 192–222.
O'Neill, H.S., Wall, V., 1987. The olivine-orthopyroxene-spinel oxygen geobarometer, the nickel precipitation curve, and the oxygen fugacity of Earth's upper mantle. J. Petrol. 28, 1169–1191.
Paterson, M., 1982. The determination of hydroxyl by infrared absorption in quartz, silicate glasses and similar materials. Bull. Minéral. 105, 20–29.
Paterson, M.S., Olgaard, D.L., 2000. Rock deformation tests to large shear strains in torsion. J. Struct. Geol. 22, 1341–1358.
Phakey, P., Dollinger, G., Christie, J., 1972. Transmission electron microscopy of experimentally deformed olivine crystals. In: Heard, H.C., Borg, I.Y., Carter, N.L. (Eds.), Flow and Fracture of rocks, 16. American Geophysical Union.
Pieri, M., Kunze, K., Burlini, L., Stretton, I., Olgaard, D.L., Burg, J.-P., Wenk, H.-R., 2001. Texture development of calcite by deformation and dynamic recrystallization at 1000 K during torsion experiments of marble to large strains. Tectonophysics 330, 119–140.
Soustelle, V., Tommasi, A., Bodinier, J.L., Garrido, C.J., Vauchez, A., 2009. Deformation and reactive melt transport in the mantle lithosphere above a large-scale partial melting domain: the Ronda Peridotite Massif. Southern Spain. J. Petrol 50, 1235–1266.
Soustelle, V., Tommasi, A., Demouchy, S., Ionov, D., 2010. Deformation and fluid-rock interactions in supra-subduction mantle: microstructures and water contents in peridotite xenoliths from the Avacha volcano, Kamchatka. J. Petrol. 51, 363–394.
Tommasi, A., Mainprice, D., Canova, G., Chastel, Y., 2000. Viscoplastic self-consistent and equilibrium-based modeling of olivine lattice preferred orientations: Implications for the upper mantle seismic anisotropy. J. Geophys. Res. 105 (B4), 7893–7908.
Vauchez, A., 1987. The development of discrete shear-zones in granite: stress, strain and changes in deformation mechanisms. Tectonophysics 133, 137–156.
Vauchez, A., Tommasi, A., Mainprice, D., 2012. Faults (shear zones) in the Earth's mantle. Tectonophysics, accepted for publication.
Wimmer, E., Wolf, W., Sticht, J., Saxe, P., 2008. Temperature-dependent diffusion coefficients from ab initio computations: hydrogen, deuterium, and tritium in nickel. Phys. Rev. B 77, 134305.
Zhao, Y.-H., Ginsberg, S., Kohlstedt, D., 2004. Solubility of hydrogen in olivine: dependence on temperature and iron content. Contrib. Mineral. Petrol. 147 (2), 155–161.
Zimmerman, M.E., Kohlstedt, D.L., 2004. Rheological properties of partially molten lherzolite. J. Petrol. 2, 275–298.